Imaging Electron Wave Functions of Quantized Energy Levels in Carbon Nanotubes

where α_n and α_s are proportional to electronic (kinetic) energies in the normal and SC states. In our experiments, ρ_s and $[N_n - N_s]$ are obtained independently (28). Therefore, the inequality $\rho_s > [N_n - N_s]$ (Fig. 3) indicates that kinetic energy change associated with the SC transition may account for the discrepancy in spectral weight.

The change of the electronic kinetic energy at $T < T_c$ suggested by our data should be contrasted with the behavior of conventional superconductors where this effect is negligibly small. Moreover, in metallic superconductors $\rho_s - [N_n - N_s]$ ought to be negative, consistent with the experimental data for lead films (29). At least two models proposed for high-T_c superconductors (17, 18) predicted the correct sign of the effect but expected it to be dominant in the response of the CuO_2 planes. The interlayer tunneling (ILT) theory (5, 8, 9) predicted the $\rho_s > [N_n - N_s]$ inequality found in the c-axis transport, but the absolute value of ρ_s in Tl2201 is smaller (7, 20) than is expected within the ILT model (5, 8). Because change in the interlayer kinetic energy has been detected in several classes of high-T_c superconductors, we believe that this unusual effect will be instrumental in narrowing the field of plausible theoretical models of high-T_c superconductivity.

References and Notes

1. S. L. Cooper and K. E. Gray, in *Physical Properties of High-Temperature Superconductors IV*, D. M. Ginsberg, Ed. (World Scientific, Singapore, 1994), pp. 61–188.
2. K. Tamasaku, Y. Nakamura, S. Uchida, *Phys. Rev. Lett.* **69**, 1455 (1992); S. Uchida, K. Tamasaku, S. Tajima, *Phys. Rev. B* **53**, 14558 (1996).
3. C. C. Homes, T. Timusk, R. Liang, D. A. Bonn, W. N. Hardy, *Phys. Rev. Lett.* **71**, 1645 (1993).
4. D. N. Basov, T. Timusk, B. Dabrowski, J. D. Jorgensen, *Phys. Rev. B* **50**, 3511 (1994).
5. P. W. Anderson, *Science* **268**, 1154 (1995); P. W. Anderson, *The Theory of Superconductivity in the High-Tc Cuprates* (Princeton Univ. Press, Princeton, NJ, 1998); P. W. Anderson, *Phys. C* **11**, 185 (1991).
6. J. Schutzmann *et al.*, *Phys. Rev. B* **55**, 11118 (1997).
7. K. Moler, J. R. Kirtley, D. G. Hinks, T. W. Li, M. Xu, *Science* **279**, 1193 (1998).
8. P. W. Anderson, *ibid.*, p. 1196.
9. S. Chakravarty, *Eur. Phys. J.* **B5**, 337 (1998).
10. E. H. Kim, *Phys. Rev. B* **58**, 2452 (1998).
11. Y. Nakamura and S. Uchida, *ibid.* **47**, 8369 (1993); K. Takenaka, K. Mizuhashi, H. Takagi, S. Uchida, *ibid.* **50**, 6534 (1994); J. Schutzmann, S. Tajima, S. Miyamoto, S. Tanaka, *Phys. Rev. Lett.* **174**, 174 (1994); R. J. Radtke and K. Levin, *Phys. C* **250**, 282 (1995); A. A. Abrikosov, *Phys. Rev. B* **54**, 12003 (1996); A. J. Leggett, *Science* **274**, 587 (1996); S. E. Shafranjuk, M. Tachiki, T. Yamashita, *Phys. Rev. B* **55**, 8425 (1997); S. Das Sarma and E. H. Hwang, *Phys. Rev. Lett.* **80**, 4752 (1998); C. Bernhard *et al.*, *ibid.*, p. 1762.
12. D. N. Basov, H. A. Mook, B. Dabrowski, T. Timusk, *Phys. Rev. B* **52**, R13141 (1995).
13. C. C. Homes, T. Timusk, D. A. Bonn, R. Liang, W. N. Hardy, *Phys. C* **254**, 265 (1995).
14. S. Tajima *et al.*, *Phys. Rev. B* **55**, 6051 (1997).
15. H. Shibata and T. Yamada, *ibid.* **56**, 14275 (1997).
16. This definition of ρ_s implies that it has dimensions of the plasma frequency squared (cm^{-2}).
17. J. E. Hirsch, *Phys. C* **199**, 305 (1992); J. E. Hirsch, *ibid.* **201**, 347 (1992).
18. A. J. Leggett, *J. Phys. Chem. Solids*, in press.
19. In underdoped Y123 crystals one finds a step-like structure at 200 to 300 cm^{-1} (3). This step-like structure is not found in La214 or Tl2201 crystals.
20. A. Tsvetkov *et al.*, *Nature* **395**, 360 (1998).
21. V. J. Emery and S. A. Kivelson, unpublished.
22. M. Tinkham and R. A. Ferrell, *Phys. Rev. Lett.* **2**, 331 (1959).
23. In Fig. 3 the spectra of $[N_n(\omega) - N_s(\omega)]/\rho_s$ for Tl2201 and La214 are shown in two different forms. Thick lines show only the electronic contribution. In these spectra the contribution of phonons has been subtracted by fitting the phonon peaks in $\sigma_1(\omega)$ to Lorentzian oscillators. Thin lines show the data without phonon subtraction. In the case of Tl2201 and La214 crystals, phonon subtraction is well-justified because all the phonon peaks are narrow and show only weak asymmetry. In the case of $YBa_2Cu_3O_{6.6}$ a broad mode at 400 cm^{-1} appears that is very different from typical phonons in the conductivity spectra of crystalline solids (3). Therefore, the phonon contribution has not been removed. The narrowing and shift of the phonon modes produce strong oscillations in the spectrum of $[N_n(\omega) - N_s(\omega)]/\rho_s$ of all the crystals. The total oscillator strength of phonons is constant with temperature. Thus, the magnitude of $[N_n(\omega) - N_s(\omega)]/\rho_s$ in the high-frequency part of the spectrum characterizes the change in the electronic part of the conductivity relative to the strength of the SC δ function.
24. Z.-X. Shen *et al.*, *Science* **267**, 343 (1995); Ding *et al.*, *Nature* **382**, 51 (1996).
25. As mentioned above, in the La214 and Y123 materials N_{eff} at $T \simeq T_c$ is depressed compared with N_{eff} at $T = 300$ K, with spectral weight transferred from the far-IR to higher energies. Only in the case of the large La214 crystals was it possible to verify experimentally that Eq. 2 is obeyed and that the weight removed from the far-IR is recovered at $\omega > 0.5$ eV (12). In all other cases the minuscule size of single crystals precluded measurements in the mid-IR with the required accuracy. It appears that below T_c some of the high-energy spectral weight (21) is recovered under the superconducting δ function, whereas far-IR conductivity in the region related to the energy gap shows only a small depression below T_c. Because the reduction of the low-energy spectral weight at $T > T_c$ is well documented for both underdoped La214 and Y123 compounds (3, 4, 14), we believe that the suppression of $\sigma_1(\omega)$ at $T < T_c$ in these materials may be unrelated to superconductivity. Instead, the diminishing of $\sigma_1(\omega)$ below T_c can be attributed at least partially to the same process that leads to transfer of the spectral weight to higher energies in the pseudogap state at $T > T_c$. Alternatively, one would be forced to assume that development of the pseudogap is suddenly interrupted at $T = T_c$; this conflicts with studies of thermodynamic properties and of nuclear magnetic resonance, both of which display continuous behavior in the underdoped cuprates across T_c [J. W. Loram *et al.*, *Phys. Rev. Lett.* **71**, 1740 (1993); W. W. Warren Jr. *et al.*, *ibid.* **62**, 1193 (1989); R. E. Walstedt *et al.*, *Phys. Rev. B* **41**, 9574 (1990)]. Therefore, a 50% contribution of mid-IR frequencies to the spectral weight of the SC δ function should be regarded as a lower limit because arguments based on the continuity of the pseudogap development at T_c appear to indicate even stronger discrepancy between ρ_s and $[N_n - N_s]$, at least in the La214 and Y123 compounds. Our room temperature data for Tl2201 do not extend below 60 cm^{-1}, and the evolution of the electronic spectral weight at $T > T_c$ in this material requires further study.
26. E. J. Singley, D. N. Basov, G. Villard, A. Maignan, unpublished data.
27. P. F. Maldague, *Phys. Rev. B* **16**, 2437 (1977).
28. It was emphasized by Chakravarty that the normal state conductivity in Eqs. 3 and 5 has to be obtained at $T \to 0$ because some of the changes in $\sigma_1(\omega)$ at $T < T_c$ can be unrelated to superconductivity (9). This correct application of sum rules to the analysis of the IR data may further enhance the inequality between ρ_s and $[N_n - N_s]$.
29. L. H. Palmer and M. Tinkham, *Phys. Rev.* **165**, 588 (1968). The authors suggest that strong coupling effects account for most of the observed discrepancy between ρ_s and $[N_n - N_s]$.
30. We are grateful to J. E. Hirsch, S. Chakravarty, V. N. Muthukumar, T. Timusk, and V. J. Emery for valuable discussions. The work at the University of California at San Diego and Brookhaven was supported by the Department of Energy (DOE), Division of Materials Sciences, under contract DE-AC02-98CH10886; the Sloan Foundation; the Research Corporation; and AFOSR grant F4962-092-J0070. The work at Argonne was supported by National Science Foundation grant DMR 91-20000 and by DOE contract W-31-109-ENG-38.

Imaging Electron Wave Functions of Quantized Energy Levels in Carbon Nanotubes

Liesbeth C. Venema, Jeroen W. G. Wildöer, Jorg W. Janssen, Sander J. Tans, Hinne L. J. Temminck Tuinstra, Leo P. Kouwenhoven, Cees Dekker*

Carbon nanotubes provide a unique system for studying one-dimensional quantization phenomena. Scanning tunneling microscopy was used to observe the electronic wave functions that correspond to quantized energy levels in short metallic carbon nanotubes. Discrete electron waves were apparent from periodic oscillations in the differential conductance as a function of the position along the tube axis, with a period that differed from that of the atomic lattice. Wave functions could be observed for several electron states at adjacent discrete energies. The measured wavelengths are in good agreement with the calculated Fermi wavelength for armchair nanotubes.

Carbon nanotubes are molecular wires that exhibit fascinating electronic properties (1). Electrons in these cylindrical fullerenes are confined in the radial and circumferential directions and can only propagate in the direction of the tube axis. Nanotubes are therefore interesting systems for studying the quantum behavior of electrons in one dimen-

sion (1D). Limiting the length of a carbon nanotube leads to a "particle-in-a-box" quantization of the energy levels. Such discrete energy levels have been observed in transport experiments on individual nanotubes and ropes (*2, 3*). The electron wave functions corresponding to these discrete states can in principle be imaged by scanning tunneling microscopy (STM). The well-known STM work on quantum corrals demonstrated that wave patterns could be directly imaged in the local density of states of a 2D metal surface (*4*). Here, we applied this technique to map out the wave functions of single molecular orbitals in short metallic carbon nanotubes. Electronic wave functions were apparent from periodic oscillations in the low-bias differential conductance along the tube axis.

Previous STM spectroscopy studies were done at a large (~2 eV) energy scale to investigate the band structure of nanotubes (*5, 6*). These experiments confirmed the prediction (*7*) that carbon nanotubes can be semiconducting or metallic, depending on the tube diameter and the chiral angle between the tube axis and hexagon rows in the atomic lattice. Here, our focus is on the low-energy (~0.1 eV) features of short metallic nanotubes that exhibit quantum size effects. Single-wall nanotubes with a diameter of ~1.4 nm were deposited on Au(111) substrates (*5, 8*). On most tubes, we were able to obtain STM images with atomic resolution (*5*), which allowed us to determine the chiral angle and diameter of the tubes (*9*). The nanotube in Fig. 1B is identified as an armchair tube by the good fit between the observed hexagon structure and the overlay of the graphene lattice. Armchair tubes have a nonchiral structure because the hexagon rows are parallel to the tube axis. This type of tube has metallic properties (*7*). Current-voltage (*I-V*) characteristics measured up to ±0.5 V on the armchair tube in Fig. 1B indeed demonstrate the simple linear behavior expected for a metallic tube. Such *I-V* measurements are done by keeping the STM tip stationary above the nanotube, switching off the feedback, and recording the current as a function of the voltage applied to the sample. In all our experiments, the STM was operated at 4.2 K (*10*).

The armchair tube in Fig. 1B was shortened to a length of ~30 nm by locally cutting the tube; this was done by applying a voltage pulse of +5 V to the STM tip at a position 30 nm from the end of the tube (*11*). STM spectroscopy was then carried out near the middle of the short tube. *I-V* curves for the

shortened nanotube show a step-like behavior (Fig. 2A), which we ascribe to quantum size effects. Steps in *I-V* correspond to quantized energy levels entering the bias window when the voltage is increased. Current steps at a voltage *V* thus correspond to discrete electron states at energy $E = E_F + \alpha eV$, where E_F is the Fermi energy, *e* is the electron charge, and $\alpha \simeq 1$ (*12*). The experimentally observed width of the current plateaus between the steps ranges from 0.05 to 0.09 V. The plateau width is determined by the total energy required to add an electron to the tube. This addition energy consists of a combination of finite-size level splitting and the Coulomb charging energy that is due to the small capacitance of the tube. A simple estimate for the energy level splitting for a tube of length $L = 30$ nm is given by $\Delta E = hv_F/2L = 0.06$ eV, where $v_F = 8.1 \times 10^5$ m/s is the Fermi velocity and *h* is Planck's constant. The capacitance *C* of a nanotube lying on a metallic substrate can be approximated by the formula for a metallic wire parallel to a conducting plane, $C = 2\pi\varepsilon_0 L/\ln\{[d + (d^2 - R^2)^{1/2}]/R\}$ (*13*), where $\varepsilon_0 = 8.85 \times 10^{-12}$ F/m, *d* is the distance from the wire axis to the plane, and $R = 0.65$ nm is the wire radius. Estimating $d \approx 0.9$ nm gives $C \approx 2.0$ aF, which yields a charging energy $E_c = e^2/C = 0.08$ eV. Both numbers are in the same range as the observed plateau width. Because the charging

energy and level splitting are of about equal magnitude, an irregular step spacing in the *I-V* curve is expected (*14*). Here, the relevant point is that each step corresponds to a discrete energy level entering the bias window.

The central result of our experiments is that the tunneling conductance measured for such discrete states is found to oscillate along the length direction of the nanotube with a period different from the atomic lattice constant. *I-V* spectroscopy curves were obtained at different locations on top of the nanotube along a line parallel to the tube axis in constant-current mode. At every point, spaced 23 pm apart, the feedback was switched off to take an *I-V* curve, starting at the bias voltage used for feedback in the constant-current mode. Figure 2A shows several *I-V* curves obtained in this way at different positions. The current displays a clear variation between maximum (dashed curves) and minimum values (solid curves) for negative bias voltage. Peaks in the differential conductance *dI/dV* (Fig. 2B) appear at the voltage positions of current steps in the *I-V* curves. The
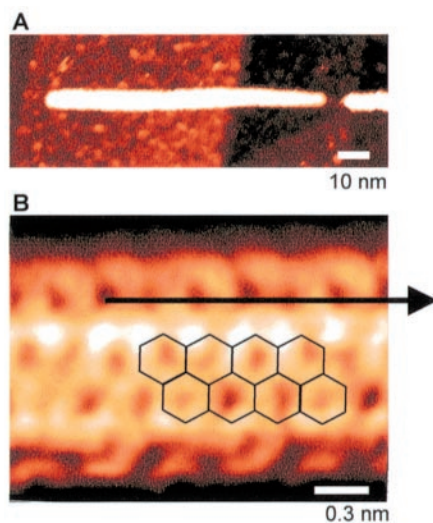
Fig. 1. STM topographic images of individual single-wall carbon nanotubes. (**A**) Example of a nanotube shortened by applying a voltage pulse to the STM tip above the tube (*11*). (**B**) Atomically resolved image of an armchair nanotube. The arrow denotes the direction of the tube axis. This nanotube can be identified as armchair-type because the hexagon rows run parallel to the direction of the tube axis (see overlay of the graphene lattice). The tube diameter is 1.3 nm. This image was taken before the tube was shortened to 30 nm. Feedback parameters are $V = 0.1$ V, $I = 20$ pA. Images were taken in constant-current mode.
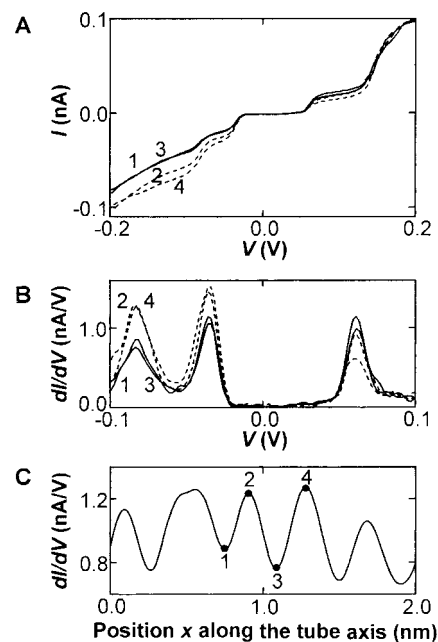
Fig. 2. STM spectroscopy measurements on a 30-nm-long armchair tube. (**A**) *I-V* characteristics of the tube shown in Fig. 1B, taken at positions about 0.18 nm apart [data points 1 to 4 in (C)] on a straight line along the tube axis. Current steps correspond to discrete energy states entering the bias window. Dashed curves, maximum values; solid curves, minimum values. (**B**) Differential conductance *dI/dV* versus *V*, as calculated from the *I-V* curves. Peaks appear at the voltage positions of current steps in the *I-V* curves. (**C**) Differential conductance *dI/dV* as a function of position along the tube. Data were taken at a bias voltage of −0.08 V. Data points 1 to 4 indicate the positions at which the four *I-V* curves plotted in (A) and *dI/dV* curves in (B) were obtained.

Department of Applied Physics and DIMES, Delft University of Technology, Lorentzweg 1, 2628 CJ Delft, Netherlands.

*To whom correspondence should be addressed. E-mail: dekker@qt.tn.tudelft.nl

height of the dI/dV peaks varies periodically with position x along the tube axis (Fig. 2C). The period of these oscillations in the differential conductance is ~0.4 nm, which clearly differs from the lattice constant of 0.25 nm. The periodic variation of dI/dV versus x can be attributed to the electronic wave functions in the nanotube, as discussed below.

The wave functions of several adjacent energy levels can be displayed simultaneously by plotting the differential conductance dI/dV as a function of the voltage and the position x along the tube (Fig. 3A). Wave patterns can be observed for four different energy levels appearing at bias voltages of 0.11, 0.04, 0.00, and −0.05 V [15]. At each level, a horizontal row of about seven maxima is resolved in dI/dV as a function of position x along the tube (see Fig. 3B for the 1D spatial profile of the wave functions belonging to these states). The experimental quantity dI/dV is a measure of the squared amplitude of the quantized electron wave function $|\Psi(E,x)|^2$ [16]. The curves in Fig. 3B are fitted with a function of the form $dI/dV = A \sin^2(2\pi x/\lambda + \phi) + B$, which represents a simple trial function for $|\Psi(E,x)|^2$. The separation of ~0.4 nm between peaks in dI/dV corresponds to half the wavelength λ because dI/dV measures the square of the wave function. The wavelengths obtained from the fitting procedure vary from 0.66 to 0.76 nm (Fig. 3B). Other measurements on the same tube reproduced values for λ in the range of 0.65 to 0.8 nm. From repeated spectroscopy measurements (such as Fig. 3A) on the same tube, we estimate the error in the wavelength to be ~0.02 nm.

Note that the dI/dV maxima in Fig. 3A occur at different positions x for the different horizontal rows. This excludes many experimental artifacts (such as, for example, oscillations in the STM) and provides compelling evidence for the interpretation in terms of standing electron waves. Typically, only a small number of discrete levels (about four) were observed around zero bias. At larger bias voltages beyond the images shown here, peaks in dI/dV could no longer be discerned clearly. At these voltages, the broadening of energy states apparently exceeds their separation. Similar electron waves with a wavelength of ~0.7 nm were also observed in a number of other shortened metallic nanotubes. On shortened semiconducting nanotubes, the level splitting could not be resolved, and attempts to measure electron waves were unsuccessful. A small energy level splitting is indeed expected for semiconducting tubes, because here the Fermi energy is located at the top of a band [7].

Figure 3C shows the topographic height profile from the constant-current measurement at +0.3 V, which clearly has a different periodicity from that observed in dI/dV (Fig. 3B). The period of 0.25 nm is in agreement with the atomic lattice constant $a_0 = 0.246$ nm for an armchair nanotube. Apparently we are imaging the atomic corrugation at high bias voltage. Simultaneously, I-V spectroscopy curves are measured at every point (Fig. 3, B and C), starting at the set point used for feedback (100 pA and +0.3 V). As a result of maintaining feedback at this voltage, the lattice periodicity is largely compensated because the STM tip follows the atomic corrugation, which makes it possible to resolve the quantized electron waves in Fig. 3, B and C [16].

Discrete levels are probed at energies near the Fermi energy E_F, and therefore the wavelength of the electron waves is close to the Fermi wavelength λ_F. Electronic band structure calculations [1, 7] for armchair tubes yield two bands near E_F with a linear energy dispersion $E(k) = E_F \pm \hbar v_F(k - k_F)$, where $\hbar = h/2\pi$, $k = 2\pi/\lambda$ is the wave vector, and $k_F = 2\pi/\lambda_F$ is the Fermi wave vector. In undoped nanotubes, the two bands cross at the Fermi energy where $k = k_F = 2\pi/3a_0$. This yields $\lambda_F = 3a_0 = 0.74$ nm, independent of the length of the tube. For nanotubes on Au(111), however, E_F is shifted away from the crossing point to lower energy by $\delta E = 0.3$ eV. This is due to charge transfer as a

Fig. 3. Spectroscopy and topography line scans along the nanotube, showing electron wave functions of discrete electron states as well as the atomic lattice. (**A**) Differential conductance dI/dV (in color scale) against the bias voltage (y axis) and the position on a straight line along the tube (x axis). This plot results from about 100 I-V curves taken at positions ~23 pm apart along the tube axis. Electron wave functions of four different energy levels are observed as periodic variations in dI/dV along the tube at voltages of 0.11, 0.04, 0.00, and −0.05 V. A horizontal row of about seven dI/dV maxima is observed at each energy level. Note that the exact voltages at which the peaks in dI/dV appear in Figs. 2 and 3A are different [15]. (**B**) dI/dV profiles at the four resolved energy levels. Fits of the function $dI/dV = A \sin^2(2\pi x/\lambda + \phi) + B$ are plotted as dashed curves. The resulting wavelengths λ are given above the curves on the right. Curves are vertically offset for clarity. (**C**) Topographic height profile $z(x)$ of the nanotube. STM topographic imaging and spectroscopy were performed simultaneously by scanning the tip along the tube and recording both the tip height (with feedback on) and I-V spectroscopy curves (feedback off). Feedback parameters are $V = 0.3$ V, $I = 100$ pA.
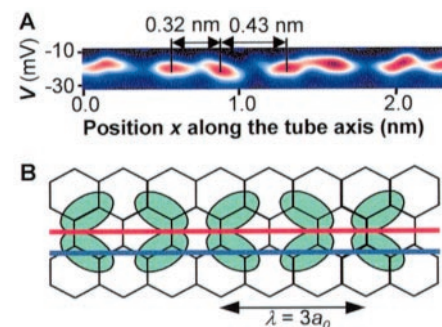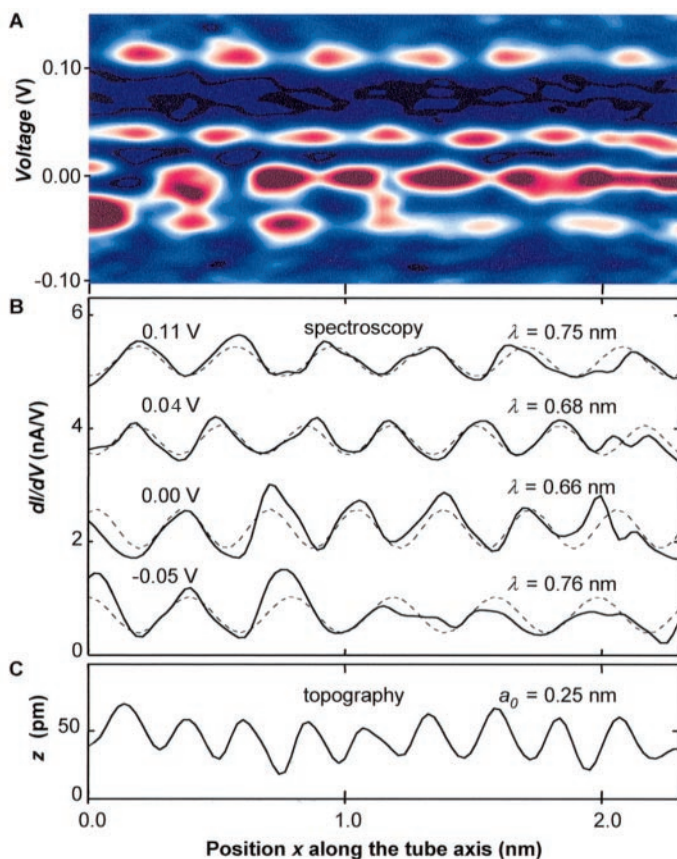
Fig. 4. Pairing of conductance peaks. (**A**) Spectroscopy line scan where pairing of dI/dV maxima can be observed. Neighboring peaks are nonequidistant, indicating a nonsinusoidal wave function. The distance between next-nearest-neighbor peaks is ~0.75 nm, which agrees with the Fermi wavelength. (**B**) Schematic of a possible arrangement of lobes of the wave function of a single molecular orbital. In a line scan along the blue line, peaks in dI/dV will be equidistant, whereas pairing will occur if a line scan is carried out along the red line.

result of a difference in work function with the underlying substrate (5). This shifts k_F to $k_F \pm \delta k$ with $\delta k = \delta E/\hbar v_F$, and λ_F thus becomes $(2\pi)/(k_F \pm \delta k) = 0.69$ nm (+) or 0.79 nm (–). The experimentally observed wavelengths (Fig. 3B) correspond well to the theoretical values, confirming the predicted band structure with two linear bands crossing near E_F. This result provides quantitative evidence for our interpretation of the oscillations in dI/dV in terms of wave functions of discrete electron states.

A short metallic nanotube resembles the textbook model for a particle in a 1D box. For a discrete energy state with quantum number n, the corresponding wavelength $\lambda_n = 2L/n$. The observed wavelength is much smaller than the tube length, in accordance with the fact that the number of electrons within one nanotube band is large ($n \sim 10^2$). The wavelength will therefore vary only slightly ($\Delta\lambda_n = \lambda_n/n \sim 0.01$ nm) for adjacent discrete energy levels in one band.

The measurements reported here are technically challenging because they require a large series of reproducible $I-V$ curves. Occasionally, we were able to resolve some of the spatial structure in the wave function at a length scale smaller than the Fermi wavelength (Fig. 4A). In this scan the peak spacing is nonequidistant, leading to an apparent pairing of peaks. This feature indicates that the wave function does not conform to a simple sinusoidal form. Recent calculations by Rubio *et al.* (*17*) indicate a nontrivial spatial variation of the nodes in the wave function of discrete electron states in the direction perpendicular to the tube axis (Fig. 4B). Line profiles can show either pairing or an equidistant peak spacing, depending on the exact position of the line scan. The observation of pairing confirms that the relevant period in the line scans is the distance between next-nearest-neighbor peaks.

Our experiments demonstrate that individual wave functions corresponding to the quantized energy levels in a short metallic nanotube can be resolved because of the large energy level splitting. The technique for recording the wave periodicity at different energy states provides a tool for further exploration of the dispersion relation in nanotubes. Future work should include similar experiments on nanotubes with various chiral angles. The methodology presented here also opens up the possibility of obtaining full 2D spatial maps of the electron wave functions in carbon nanotubes.

References and Notes

1. M. S. Dresselhaus, G. Dresselhaus, P. C. Eklund, *Science of Fullerenes and Carbon Nanotubes* (Academic Press, San Diego, CA, 1996).
2. M. Bockrath *et al.*, *Science* **275**, 1922 (1997).
3. S. J. Tans *et al.*, *Nature* **386**, 474 (1997).
4. M. F. Crommie, C. P. Lutz, D. M. Eigler, *Science* **262**, 218 (1993); *Nature* **363**, 424 (1993); Y. Hasegawa and Ph. Avouris, *Phys. Rev. Lett.* **71**, 1071 (1993).
5. J. W. G. Wildöer, L. C. Venema, A. G. Rinzler, R. E. Smalley, C. Dekker, *Nature* **391**, 59 (1998).
6. T. W. Odom, J.-L. Huang, P. Kim, C. M. Lieber, *ibid.*, p. 62.
7. J. W. Mintmire, B. I. Dunlap, C. T. White, *Phys. Rev. Lett.* **68**, 631 (1992); N. Hamada, S.-I. Sawada, A. Oshiyama, *ibid.*, p. 1579; R. Saito, M. Fujita, G. Dresselhaus, M. S. Dresselhaus, *Appl. Phys. Lett.* **60**, 2204 (1992).
8. A. Thess *et al.*, *Science* **273**, 483 (1996).
9. Exact identification of the lattice indices (n,m) [see (*1*)] of chiral nanotubes is quite difficult because both the nanotube diameter and the chiral angle between hexagon rows and the tube axis must be measured with high accuracy. The (n,m) indices are crucial for chiral tubes because a minor change in one of these determines whether the tube is a metal or a semiconductor. For armchair tubes, however, the situation is easier. The nonchiral structure with hexagon rows running parallel to the tube axis can be easily observed from the atomically resolved images, and a precise determination of the diameter is not essential because armchair tubes of all diameters are metallic.
10. J. W. G. Wildöer, A. J. A. van Roij, H. van Kempen, C. J. P. M. Harmans, *Rev. Sci. Instrum.* **65**, 2849 (1994). In our setup the lateral drift is almost negligible (typically <1 nm per hour) because the STM is cooled in a ^{4}He bath cryostat. Successive STM spectroscopy line scans therefore show identical results. Over a longer period, however, the tip may change position slightly as a result of residual drift or minor changes in the tip.
11. L. C. Venema *et al.*, *Appl. Phys. Lett.* **71**, 2629 (1997). After this cutting event, the tip was cleaned by applying voltage pulses above the gold substrate, far away from the tube. Linear $I-V$ spectroscopy curves on clean areas of the gold substrate demonstrated that the tip was free of debris.
12. The applied voltage is in principle divided into a part that drops over the tunnel gap and a part that drops between the nanotube and the substrate. The ratio α between these voltages is determined by the capacitance ratio. Because the capacitance between nanotube and substrate is much larger than that between the nanotube and the STM tip, the voltage will drop almost entirely over the tunnel gap, and accordingly α has a value close to 1.
13. W. T. Scott, *The Physics of Electricity and Magnetism* (Wiley, New York, ed. 2, 1966), pp. 163–165.
14. L. P. Kouwenhoven *et al.*, in *Mesoscopic Electron Transport*, L. L. Sohn, G. Schön, L. P. Kouwenhoven, Eds. (Kluwer, Dordrecht, Netherlands, 1997), pp. 105–214.
15. Note that the exact voltages at which the peaks in dI/dV appear in Figs. 2 and 3A are different. This can be attributed to variations in the offset charge caused by trapping of charge in the environment of the tube, as is well known in Coulomb charging phenomena [see R. Wilkins and R. C. Jaclevic, *Phys. Rev. Lett.* **63**, 801 (1989); J. G. A. Dubois, E. N. G. Verheijen, J. W. Gerritsen, H. Van Kempen, *Phys. Rev. B* **48**, 11260 (1993)]. Variation of the offset charge may change the Coulomb gap and thus shift the exact voltage at which the discrete levels of the tube appear in the $I-V$ measurements. In fact, switching of offset charges was observed in some of our line scans. This effect is irrelevant for the observations reported here, which are the periodic oscillations in the differential conductance of discrete energy levels.
16. The total wave function is in fact defined by the atomic lattice potential modulated with a standing wave profile resulting from the confinement in the length direction. Because the STM tip follows the atomic corrugation by scanning in constant-current mode at a high bias voltage, the lattice periodicity is largely compensated so that the standing waves can be resolved in the spectroscopy measurements for several discrete states at low bias.
17. A. Rubio, E. Artacho, P. Ordejon, P. D. Sanchez-Portal, D. J. Soler, in preparation.
18. We thank R. E. Smalley and co-workers for supplying the nanotube material and A. Rubio for sharing results before publication. Supported in part by the Dutch Foundation for Fundamental Research of Matter (FOM). L.P.K. is supported by the Royal Dutch Acadamy of Sciences and Art (KNAW).

DOAS Measurements of Tropospheric Bromine Oxide in Mid-Latitudes

Kai Hebestreit, Jochen Stutz,* David Rosen, Valery Matveiv, Mordechai Peleg, Menachem Luria, Ulrich Platt

Episodes of elevated bromine oxide (BrO) concentration are known to occur at high latitudes in the Arctic boundary layer and to lead to catalytic destruction of ozone at those latitudes; these events have not been observed at lower latitudes. With the use of differential optical absorption spectroscopy (DOAS), locally high BrO concentrations were observed at mid-latitudes at the Dead Sea, Israel, during spring 1997. Mixing ratios peaked daily at around 80 parts per trillion around noon and were correlated with low boundary-layer ozone mixing ratios.

Sudden boundary-layer ozone (O_3) depletion events during Arctic spring (*1, 2*) are likely caused by the presence of reactive halogen

K. Hebestreit, J. Stutz, U. Platt, Institut für Umweltphysik, Ruprecht-Karls-Universität Heidelberg, Im Neuenheimer Feld 366, D-69120 Heidelberg, Germany. D. Rosen, V. Matveiv, M. Peleg, M. Luria, Environmental Science, School of Applied Science, Hebrew University, 91904 Jerusalem, Israel.

*To whom correspondence should be addressed. E-mail: stu@uphys1.uphys.uni-heidelberg.de

species, particularly BrO. Bromine or BrO (or other halogens) catalytically convert two ozone molecules to three oxygen molecules without a loss of the halogen (*3*). Although the chemical cycles destroying ozone are well understood, the source of the reactive bromine compounds remains unclear, but they are most likely formed by oxidation of sea salt halogenides (*4*). Bromine oxide has been observed by DOAS in several places in the Arctic (*5, 6*) and Antarctica (*7*). Satellite-